



Chip-scale Floquet topological insulators for 5G wireless systems

Aravind Nagulu^{1,6}, Xiang Ni^{2,6}, Ahmed Kord^{1,6}, Mykhailo Tymchenko^{3,4}, Sasank Garikapati¹, Andrea Alù^{2,4,5} and Harish Krishnaswamy¹

Floquet topological insulators, which have an exotic topological order sustained by time-varying Hamiltonians, could be of use in a range of technologies, including wireless communications, radar and quantum information processing. However, demonstrations of photonic Floquet topological insulators have been limited to systems that emulate time with a spatial dimension, which preserves time-reversal symmetry and thus removes valuable features including non-reciprocal topological protection. Here we report photonic Floquet topological insulators based on quasi-electrostatic wave propagation in switched-capacitor networks. The approach provides non-reciprocal Floquet topological insulators for electromagnetic waves and opens a large topological bandgap that spans up to gigahertz frequencies. Our devices exploit time modulation to operate beyond the delay-bandwidth limit of conventional linear time-invariant electromagnetic structures and therefore offer large delays, despite the broad bandwidth. The Floquet topological insulator is integrated into a complementary metal-oxide-semiconductor (CMOS) chip, and we illustrate its potential for 5G wireless systems by showing that it can be used for multi-antenna full-duplex wireless operation and true-time-delay-based broadband beamforming.

Topological insulators (TIs) have an insulating response in the bulk, but act as a conductor on the boundary^{1,2}. Their conductive edge states are unidirectional and immune to reflections from surface imperfections or local disorder. These properties were originally discovered in the field of condensed-matter physics, stemming from studies on the quantum Hall effect³. Topological phenomena do not arise only in static systems but also in periodically driven quantum systems, which are referred to as Floquet TIs and whose topological order stems from external modulation^{4–6}. The Chern number, which is commonly used to characterize the topological order in static TIs, is often not sufficient to characterize the topological features of Floquet systems in their entirety, since anomalous chiral edge states may still arise when the Chern numbers of all the Floquet bands are zero. In this situation, the topological order is encoded in the microscopic details of the driving protocol rather than in the Floquet system itself⁷.

Recent works have looked to extend TI concepts from fermionic systems to bosonic counterparts^{8–11}, resulting in TIs for electromagnetic waves across a wide frequency range ranging from d.c.^{12–15} and microwave^{16–19} to optical spectra^{20–23}. The underlying principles common to these works is the idea of inducing topological order either by breaking time-reversal symmetry through magneto-optic phenomena or parametric modulation of the constituent elements, or by exploiting protected states arising from internal or spatial symmetries. The first approach has proven very effective to induce strong topological robustness, since it breaks reciprocity and guarantees the absence of reflected edge states for any type of disorder^{8,16,17,22,24,25}. Symmetry-protected topological states, on the other hand, are only immune against imperfections preserving the relevant symmetry^{19,20,23}, and hence, their robustness is inherently weaker.

Periodically driven spatiotemporal modulation can lead to Floquet topological order, offering robust non-reciprocal topological protection. Reciprocity is broken through time modulation, which is advantageous for integration and practical implementations^{21,24,25}. However, previous experimental implementations of Floquet TIs in photonics^{22,26,27} have exclusively relied on replacing time with a relevant spatial dimension, resulting in arrays of evanescently coupled optical waveguides slowly modulated in space along the direction of propagation. These systems do not explicitly break time-reversal symmetry; therefore, they cannot offer isolation and strong topological protection. In addition, they are not feasible for on-chip implementation.

Genuine Floquet TIs require the generation and distribution of phase-synchronized time modulation signals across a large array^{25,28,29}, which makes their implementation challenging. We recently reported the development of an elastodynamic Floquet TI through a complex macroscopic network of separately controlled piezoelectric resonators, but such an approach would be difficult to replicate over larger scales or in an integrated miniaturized design²⁹. Floquet TIs also typically exhibit a topologically protected bandgap limited to a narrow range of operating wavelengths, thus limiting their practical impact^{22,25–27,29–32}.

In this Article, we report a Floquet TI for electromagnetic waves—that is, a Floquet topological electromagnetic circuit—based on a network of quasi-electrostatic helicoidally rotating elements³³. The unit cells of our TI apply broadband synthetic rotation to an impinging signal in two dimensions, based on tailored spatiotemporal modulation of a switched-capacitor network supporting quasi-electrostatic signal propagation³⁴. Conventional approaches to TIs require a lattice period of the order of the wavelength to open a bandgap, leading to large footprints. In our approach, the rotation of each element is quasi-electrostatic in nature, relaxing this requirement

¹Department of Electrical Engineering, Columbia University, New York, NY, USA. ²Photonics Initiative, Advanced Science Research Center, City University of New York, New York, NY, USA. ³Lightmatter Inc., Boston, MA, USA. ⁴Department of Electrical and Computer Engineering, The University of Texas at Austin, Austin, TX, USA. ⁵Physics Program, Graduate Center, City University of New York, New York, NY, USA. ⁶These authors contributed equally: Aravind Nagulu, Xiang Ni, Ahmed Kord. ✉e-mail: aalu@gc.cuny.edu; harish@ee.columbia.edu

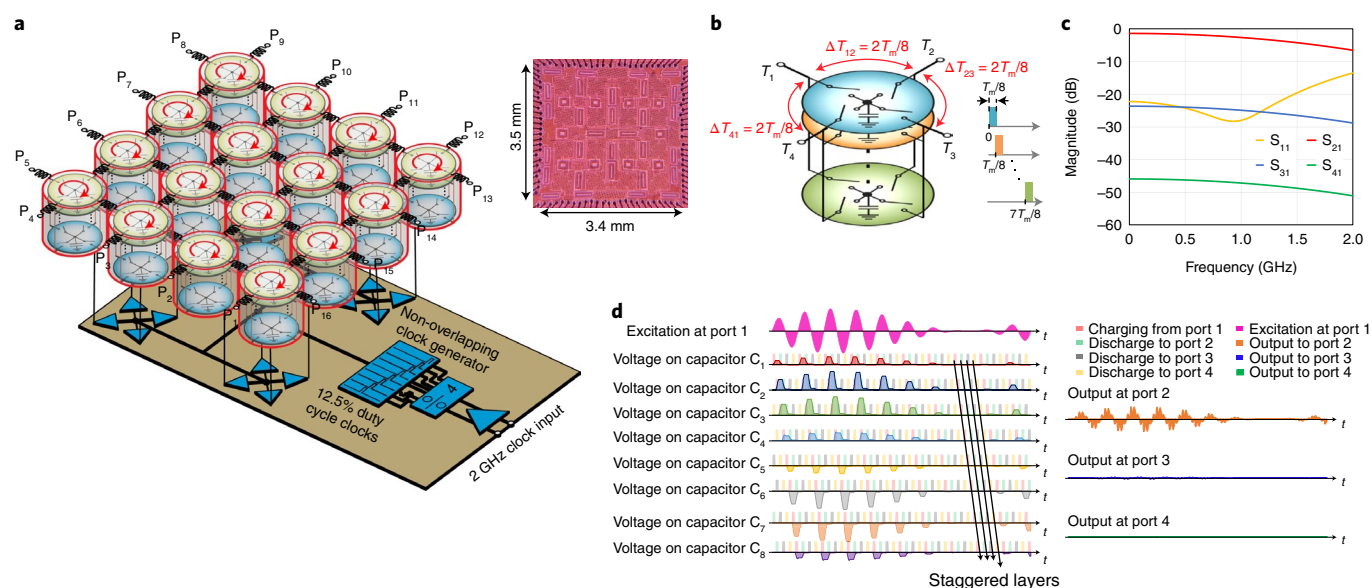


Fig. 1 | 4×4 dispersion-free Floquet TI using helicoidally rotating, quasi-electrostatic unit elements. **a**, Conceptual diagram and chip microphotograph of the Floquet TI implemented in a 45 nm silicon-on-insulator CMOS process. **b–d**, Circuit and timing diagram (**b**), simulated scattering parameters (**c**) and time-domain operation (**d**) of a four-port, eight-layer synthetically helicoidally rotating quasi-electrostatic circulator modulated at $f_m = 500$ MHz with shunt capacitors $C = 2.5$ pF and matching inductors $L = 2.5$ nH at the ports, exhibiting low-loss transmission and high isolation across a wide bandwidth.

and resulting in a subwavelength footprint for the entire Floquet lattice, as well as easier phase-synchronized modulation.

Our quasi-electrostatic design results in a frequency-independent response, which supports a topological bandgap orders of magnitude larger than previously reported photonic TI, extending from d.c. to gigahertz frequencies. The ultrabroad bandgap implies that it cannot be closed by small disorder, leading to high levels of robustness. At the same time, quasi-electrostatic wave propagation operates beyond the delay-bandwidth (DBW) limit of conventional linear time-invariant electromagnetic structures by virtue of time modulation³⁴, allowing our TI to offer large delays despite the wide bandwidth. Each lattice node, being already modulated in time through commutated switches, can be dynamically reconfigured in real time to sustain a local handedness of choice, enabling the configuration of arbitrary routing of topologically protected signals.

Our implementation provides a platform to probe the physics of topological wave propagation and to multiplex different functionalities for applications including wireless communications, radar and quantum information processing. We illustrate its functionality in a 5G wireless system, where the TI serves as a new antenna interface for a 750 MHz full-duplex (FD) phased array. The programmable delays within each lattice element enable independent phased-array beamforming in the transmit and receive modes, and its isolation features enable FD simultaneous transmission and reception of broadband radio-wave signals. The reconfigurability of our TI also allows the same device to be used as the antenna interface in an ultrawideband true-time-delay (TTD) beamforming network for impulse radars, in which reconfigurable signal routing and wideband nanosecond-scale delays enable TTD-based beamforming of ultrawideband signals spanning d.c. to gigahertz frequencies.

Dispersion-free quasi-electrostatic Floquet TI

Floquet topological order is induced in our TI (Fig. 1a) by imparting distributed deeply subwavelength, broadband helicoidal rotation through a dense array of ultrabroadband circulators³³ arranged in a square lattice. Each circulator is based on the concept of quasi-electrostatic wave propagation in switched-capacitor

networks³⁴, and consists of eight identical switched-capacitor layers connected in parallel to four ports (Fig. 1b). Each layer consists of a shunt capacitor connected to the four ports through transistor switches in a star configuration (Supplementary Section 1 provides further details on the operation of the quasi-electrostatic unit circulator).

Switches across layers associated with a given port are modulated in a staggered fashion to sequentially turn them on with no overlapping, and this scheme imparts a synthetic vertical-plane rotary motion that creates a quasi-electrostatic frequency-independent ring resonance within near-infinitesimal dimensions (Fig. 1b, timing diagram). The switches within each layer are also modulated in a staggered fashion with no overlapping, imparting a synthetic horizontal-plane rotation that applies angular-momentum biasing³⁵ to break reciprocity. The overall result is a deeply subwavelength element that effectively moves on a helicoidal path across layers, realizing N -port circulation over an extremely broad bandwidth within an infinitesimal footprint.

In Fig. 1a, each element of the lattice supports wave propagation in the clockwise (CW) direction, that is, from T_1 to T_2 , from T_2 to T_3 and so on, providing isolation between any other pair of ports. Additionally, our complementary metal-oxide-semiconductor (CMOS) chip implementation allows real-time reconfigurability of the modulation signal applied to the switches, enabling wide reconfiguration of each element between CW handedness ($T_1 \rightarrow T_2 \rightarrow T_3 \rightarrow T_4$), counter-clockwise (CCW) handedness ($T_4 \rightarrow T_3 \rightarrow T_2 \rightarrow T_1$), and in general, other hybrid switching schemes, such as ($T_1 \rightarrow T_3 \rightarrow T_2 \rightarrow T_4$) and ($T_1 \rightarrow T_4 \rightarrow T_3 \rightarrow T_2$). Figure 1c shows the simulated scattering parameters of a four-port, eight-layered circulator, modulated at $f_m = 500$ MHz. As shown in Fig. 1d, the isolation mechanism in this unit-cell architecture is due to charge-discharge through the port impedances, hence making this structure an extremely broadband alternative to previous time-modulated implementations of non-reciprocal angular-momentum devices^{35,36}, which rely on destructive interference of the signal coming through two different paths or modes. Additionally, its infinitesimal form factor is 100–1,000 times more compact than architectures based on resonators^{35,36}.

We take advantage of this synthetic helicoidal rotation and broadband non-reciprocal response at the unit-cell level to implement a chip-scale Floquet TI by connecting these elements in a 4×4 square lattice, and driving them through a common modulation clocking circuitry (Fig. 1a). When all the unit cells are configured with the appropriate handedness, the signal propagation through this lattice is analogous to the transport of an electron travelling through a two-dimensional lattice with magnetic bias applied on each atom, in which the role of magnetic bias is replaced by the angular momentum imparted by each unit cell. Hence, we expect the lattice to exhibit topological features, analogous to those envisioned elsewhere²⁵, but extended in our case over an extremely broad bandwidth and within an ultracompact, resonator-free form factor. Small inductive coupling elements between the unit cells have been added to enhance the non-reciprocal performance of the individual units³³ by enabling complete energy transfer between neighbouring elements³³, which is equivalent to complete charge transfer from one shunt capacitor to the next. Using wideband, resonator-free elements relaxes the component mismatch requirements, and it alleviates fabrication and layout challenges of an electrically large lattice of high quality factor resonators, as evident in all previous designs for Floquet TIs^{24,25,29}.

Although the deeply subwavelength dimensions of the lattice ease the modulation signal distribution, Floquet TIs are inherently prone to phase desynchronization of the modulation signal and harmonic conversion phenomena. On the contrary, our TI implementation (Supplementary Section 1C) offers substantial resilience to phase deviations in the modulation clock (up to $\pm 12.5\%$ of time period T_m).

Network theory for TIs based on resonator-free elements

Coupled-mode theory based on resonant modes cannot accurately describe our system due to the ultrabroadband nature of our dispersion-free non-reciprocal unit. We thus model our Floquet TI lattice using resonator-free Floquet network theory^{37,38}. The Floquet network model usually deals with two-port scatterers, whereas our chip-scale Floquet TI consists of four-port unit elements, whose scattering parameters are constrained by rotational symmetry, such that $s_{ji} = s_{j+1,i+1}$, where $i, j = 1-4$ represent the port numbers. To facilitate the analysis, we provide a specific choice regarding the plaquette of the network lattice, around which the field travels either in a CW or CCW pattern corresponding to CW or CCW modes, respectively. Therefore, we can treat the scattering process of the four-port circulators arranged in the network lattice as the separate scattering processes of CW (pseudo-spin-up) modes, CCW (pseudo-spin-down) modes and the mixed scattering processes (pseudo-spin couplings) between them. Notice that the choice of plaquette is arbitrary and will not alter the end result. Without the loss of generality, we rearrange the scattering equations according to the plaquette shown in Fig. 2a as follows:

$$\begin{pmatrix} B_{cw} \\ B_{ccw} \end{pmatrix} = \begin{pmatrix} S_{cw} & S_{int} \\ S'_{int} & S_{ccw} \end{pmatrix} \begin{pmatrix} A_{cw} \\ A_{ccw} \end{pmatrix}, \quad (1)$$

where the CW- and CCW-propagating fields at the incoming (outgoing) ports are represented by $A(B)_{cw} = [a_1(b_1), a_3(b_3)]^T$ and $A(B)_{ccw} = [a_2(b_2), a_4(b_4)]^T$, respectively. S_{cw} (S_{ccw}) represents the transmission in CW (CCW) handedness and S_{int} (S'_{int}) couples the CW (CCW) modes, respectively.

When the circulator is synthetically rotated with CW handedness, for example, $|s_{1+1,i}| > |s_{1+2,i}| > |s_{1+3,i}|$, the four-port scattering is equivalent to the superposition of strong coupling of CCW modes, weak coupling of CW modes, and negligible mixing of CW and CCW modes in the two-port network models (Fig. 2a). As a consequence, the dynamics of the CW-mode family map to those of

the well-known Floquet two-port network model, which support anomalous topological phase and topological edge states under the strong scattering condition. Meanwhile, the dynamics of the CCW modes map to a topologically trivial phase because of the weak scattering, and the interaction between CW and CCW modes is too weak to have a determining effect on the topology of the respective subspaces. To evaluate the topological properties of the lattice, we approximated our unit cells to be lossless and frequency independent, with negligible harmonic conversion and the scattering components s_{ji} in our quasi-electrostatic system can be approximately modelled as

$$\begin{aligned} s_{i+1,i} &\approx \left[1 - 0.5 \left(e^{-2 \frac{T_m}{NZ_0 C}} + e^{-4 \frac{T_m}{NZ_0 C}} \right) \right] e^{-i\omega_{in} \frac{T_m}{4}}, \\ s_{j,i} &\approx e^{-\{(j-i-1)\%L\} \frac{T_m}{NZ_0 C}} e^{-i\{(j-i)\%L\} \omega_{in} \frac{T_m}{4}}, j \neq i, i+1, \\ s_{i,i} &\approx 0, \end{aligned} \quad (2)$$

where ω_{in} is the input frequency, Z_0 is the port impedance, $N=8$ is the number of layers in the unit circulator, C is the shunt capacitance of each layer, $T_m = 1/f_m$, $L=4$ is the number of ports in the circulator and $\%$ represents the modulo operation (Supplementary Section 1A provides details on this modelling). In our experiments, the parameter $\frac{T_m}{NZ_0 C} = 2$, leading to strong scattering of CCW modes.

Floquet band structures are calculated for a lattice that is periodic in the x direction and has a finite length L in the y direction (Supplementary Section 2 provides the detailed calculation). Interestingly, we observe flat bands (Fig. 2b, red lines) stemming from the bulk modes arising from the trapped resonance in the plaquette of the network lattice when the phase delay meets the condition $\omega_{in} T_m = 2\pi q$, where $q = 0, 1, 2, \dots$, or equivalently $f_{in}/f_m = q$, that is, at operating frequencies that are multiples of the modulation frequency. In addition to these bulk bands, linear edge bands (Fig. 2b, blue lines) arise across the whole band structure. Since f_{in} is linearly proportional to the transmission phase that is, in turn, periodic, topological edge bands are continuously extended in the frequency dimension as long as the strong scattering condition, or equivalently, the strong circulation condition implemented in the experiment, is satisfied. Depending on the phase delay of the signal at the boundaries, topological edge states may have different group velocities from the one shown in Fig. 2b (Supplementary Section 2).

Furthermore, we carried out simulations of a finite network consisting of a 10×10 array with CW handedness and impedance-matched boundary conditions ($Z_{boundary} = Z_0$) at the bottom and right edges of the lattice. In Fig. 2d, the input port is placed at the left-bottom site of the lattice and f_{in} is swept from 0 to $2f_m$. The transmittance spectra (Fig. 2c) as a function of f_{in} are produced from the data taken in the bulk regions (Fig. 2d, dashed boxes). The transmittance is substantially larger near the bulk frequencies ($f_{in}/f_m = q$) than at other frequencies, indicating that the fields are concentrated at the edges and dissipate inside the bulk of the lattice at arbitrary frequencies, except at the bulk frequencies. Furthermore, by plotting the field distribution of the lattice (Fig. 2d), we observe that the excited fields are mostly concentrated at the right and top edges of the lattice for arbitrary f_{in} , except at and near $f_{in}/f_m = q$. In this entire frequency range, we observe signal transport in a CW-rotating pattern, stopping at the right-top corner due to the grounded boundary condition (Fig. 2d, left and right). This ultrabroadband feature arises from the linearly extended edge bands in the frequency dimension (Fig. 2b). Figure 2d, middle, shows the field distribution for $f_{in} = 0.95f_m$; besides the excitation of edge modes, both CW and CCW bulk modes are excited, and all the lattice elements have non-zero fields. Unlike topological edge states, topologically trivial circulating modes would be independent of the input frequency and the excited fields would always localize at the edges. When the

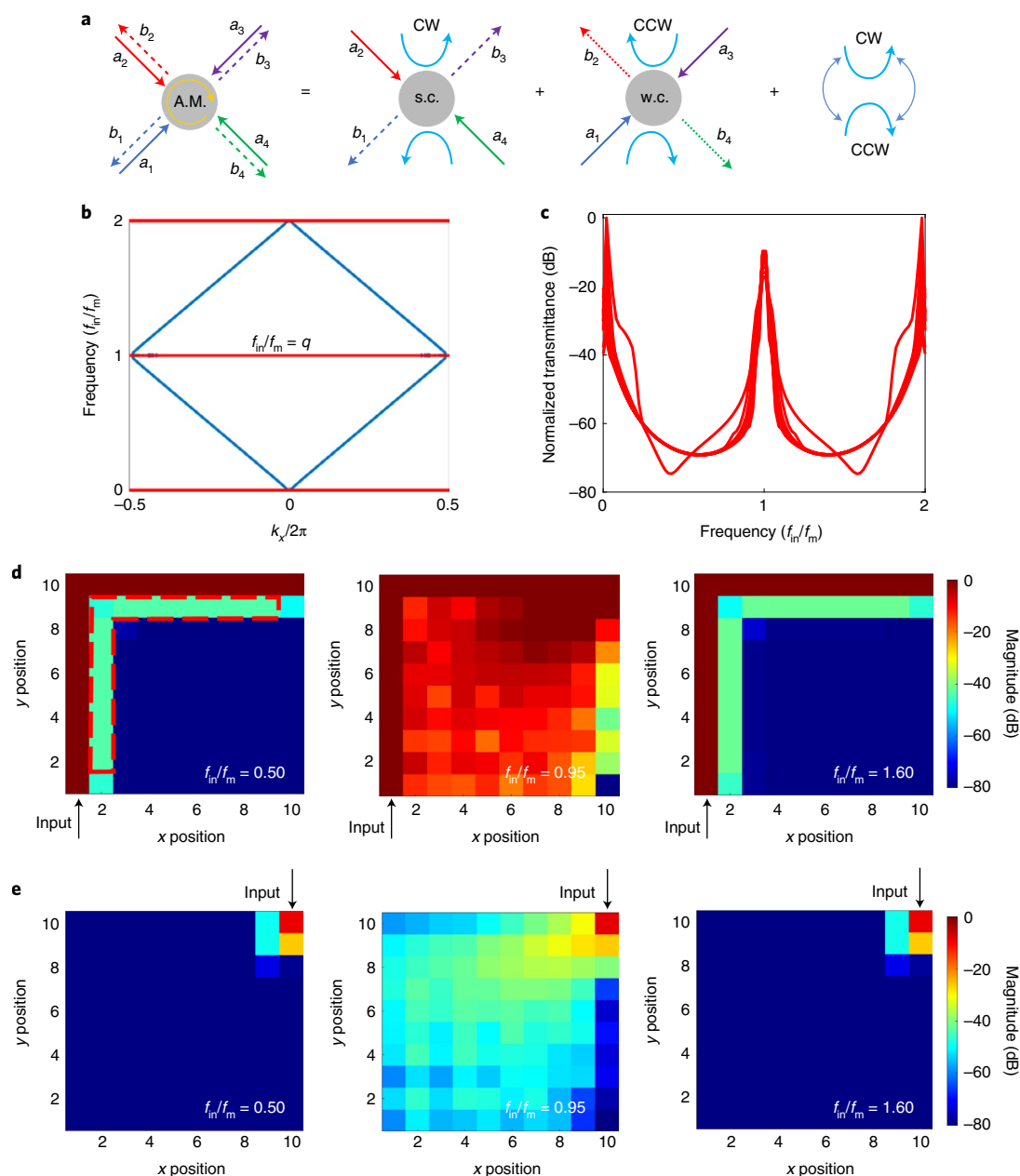


Fig. 2 | Analysis of Floquet TI lattice based on resonator-free network. **a**, Schematic showing the scattering processes of a four-port scatterer and those of two-port scatterers. A.M., angular momentum; s.c., strong coupling; w.c., weak coupling. **b**, Band structure of a supercell network formed by the four-port circulators, which consists of ten unit cells in the y direction. Bloch periodic boundaries are applied in the x direction. The red lines represent the flat bulk bands, and blue lines represent the topological edge states that are continuously extended in frequency. **c**, Transmittance spectra of the bulk at sites that are one unit cell away from the edges, indicated by the dashed red lines in **d** (left). **d, e**, Normalized field distribution of a finite network consisting of elements when the input port is placed at the left-bottom site (**d**) and the right top site (**e**). Continuous boundary conditions are applied at the upper and left edges of the lattice, and zero boundary conditions are applied at the bottom and right edges.

lattice with CW handedness is excited at the top-right corner (Fig. 2e), the fields are immediately absorbed by the boundaries at the right edge, and no field is backscattered because of the CW topological protection. This phenomenon is totally independent of f_{in}/f_m , except near $f_{\text{in}}/f_m = q$ where the signal diffuses into the bulk due to the excitation of bulk modes (Fig. 2e, middle). We emphasize that the Chern numbers of all the flat Floquet bands are zero; the non-trivial topology here arises from the strong scattering of the network lattice achieved by the CW rotation of the unit-cell elements.

We have carried out first-principles circuit simulations of a 900 element lattice (30×30), and the results closely match both our

theoretical model and our experimental results (Supplementary Section 4). In addition to the resonant-free network model, we also carried out Floquet coupled-mode analysis for square lattices based on spatiotemporally modulated angular-momentum-biased LC-resonator unit cells (Supplementary Section 3). This analysis showcases the physics of our system, mapping our frequency-independent response to the centre of the relevant band-gap in this resonant lattice. Furthermore, the LC-resonator-based Floquet TI stands in contrast to our quasi-electrostatic TI in that it exhibits far more dispersion and a far narrower bandgap, underscoring the benefits of our approach.

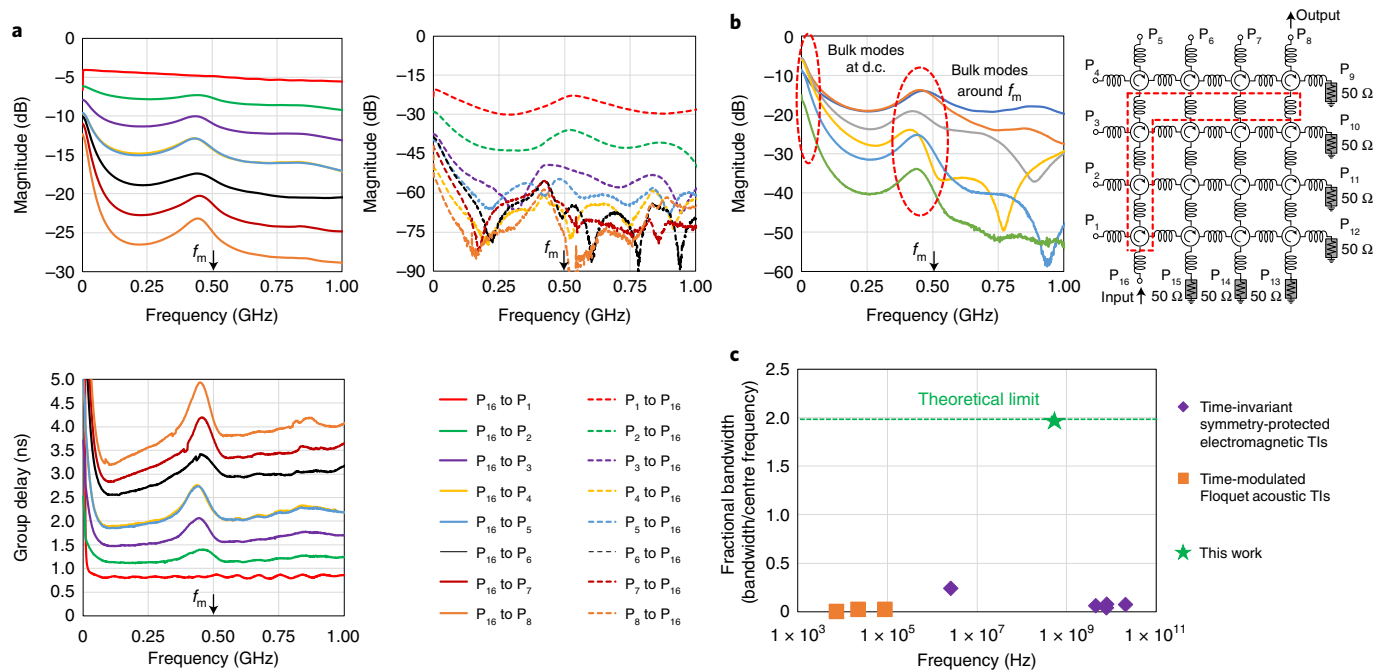


Fig. 3 | Measured scattering parameters and group delay of the Floquet TI IC. **a**, Measured CW transmission, CCW isolation and CW group delay parameters at the edge nodes (from P1 to P8) when all the unit cells are configured for CW propagation. **b**, Measured transmission at the bulk nodes that are one site away from the edge as marked using the red dashed line in the 4×4 lattice on the right. **c**, Fractional bandwidths of several earlier time-invariant symmetry-protected electromagnetic TIs, time-modulated acoustic TIs and our quasi-electrostatic chip-scale Floquet TI across their operating centre frequency.

Topological properties of 4×4 Floquet TI CMOS IC

We implemented the quasi-electrostatic Floquet TI in a 45 nm silicon-on-insulator CMOS chip. Figure 1a shows the microphotograph of our deeply subwavelength chip-scale quasi-electrostatic Floquet TI, with a size of $3.5 \text{ mm} \times 3.4 \text{ mm}$ ($\sim \lambda/860 \times \lambda/880$ at 100 MHz and $\sim \lambda/86 \times \lambda/88$ at 1 GHz). By changing the switching scheme, the lattice topology can be dynamically reconfigured locally, namely, the non-trivial topological subspace can be switched between the CW-mode and CCW-mode families, corresponding to opposite chirality of edge states when all the unit cells are configured for CW/CCW handedness, to create propagation along arbitrarily shaped domain walls between the sublattices with varied topologies, as well as to support bulk transmission if we implement the hybrid modality in each node. These functionalities are experimentally validated below, along with the utility of this TI in 5G wireless and ultrawideband impulse radar applications.

When the lattice elements are configured for CW rotation and modulated at $f_m = 500 \text{ MHz}$, the lattice exhibits an overall anomalous topological phase, and it does not support any bulk mode except at and near $f_{in} = qf_m$, as predicted by our Floquet network theory and verified by experimental results (Fig. 3). Indeed, the measured transmission spectra for CW propagation along the edge (Fig. 3a, top left) are substantially larger than those for CCW propagation (Fig. 3a, top right). The isolation accumulates along the edge in the CCW direction, increasing at a rate of $\sim 20 \text{ dB}$ per element until it reaches the chip-level parasitic limit of $60\text{--}70 \text{ dB}$. It should be noted that such a high level of isolation cannot be achieved in a single circulator unit cell due to fabrication tolerances and impedance mismatches. The use of tuning elements to enhance isolation requires real-time configuration, and can never be achieved in a single cell over such a wide bandwidth. The group delay linearly increases for CW propagation along the edge as expected (Fig. 3a, bottom left), which provides additional evidence of the emergence of topological edge states. The emergence of bulk modes is evident both in

first-principles simulations of the electrical circuit (Supplementary Section 4) and in our experimental results (Fig. 3b), in which the transmittance of bulk nodes exhibits peaks near $f_{in} = 0$ and $f_{in} = f_m$.

The ultrabroadband, dispersion-free operation of our Floquet TI is illustrated through field distributions plotted at different signal frequencies, such as $f_{in} = 0.5f_m$ and $f_{in} = 1.6f_m$ (Fig. 4a). When the signal is excited at P₁₆, the signal travels along the edge to P₈ in the CW direction and reflecting off the ports with open termination (P₁ through P₇) and not propagating in the bulk (Fig. 4a, left and right). When the frequency of the signal is chosen as $f_{in} = f_m$, the signal power decays more slowly and spreads over a larger area of the lattice compared with the previous cases, indicating the bulk states are excited, too (Fig. 4a, middle). On the other hand, when the signal is excited at P₈, it continues to travel in the CW direction and is dissipated into the absorptive terminations at ports P₉ through P₁₅, and no backscattering signal is detected at P₈ due to the topological prohibition of backward states (Fig. 4b). We also observed more diffusive spread of the signal when $f_{in} = f_m$, which further verifies the fact the bulk states are excited. Thus, the strong contrast between CW and CCW rotation (Fig. 4a,b) validates the claim of anomalous topological phase of the Floquet TI and confirms our theoretical model. Similarly, the lattice can be dynamically reconfigured to the non-trivial topology of the opposite mode family by reversing the handedness of the synthetic rotation of each unit cell.

The operational bandwidth of a system should be evaluated in comparison to the centre frequency of operation, determined using

$$\text{Fractional bandwidth} = \frac{\text{Signal bandwidth}}{\text{Centre frequency}} \times 100\%.$$

In this context, it is particularly challenging to achieve broadband operation from extremely low frequencies (near-d.c.) to high frequencies due to the wide disparity in wavelength/frequency. A device that operates from d.c. to gigahertz frequencies, as the one presented here, achieves a fractional bandwidth of 200%, which is the maximum achievable value. The topological features of our circuit offer orders of magnitude

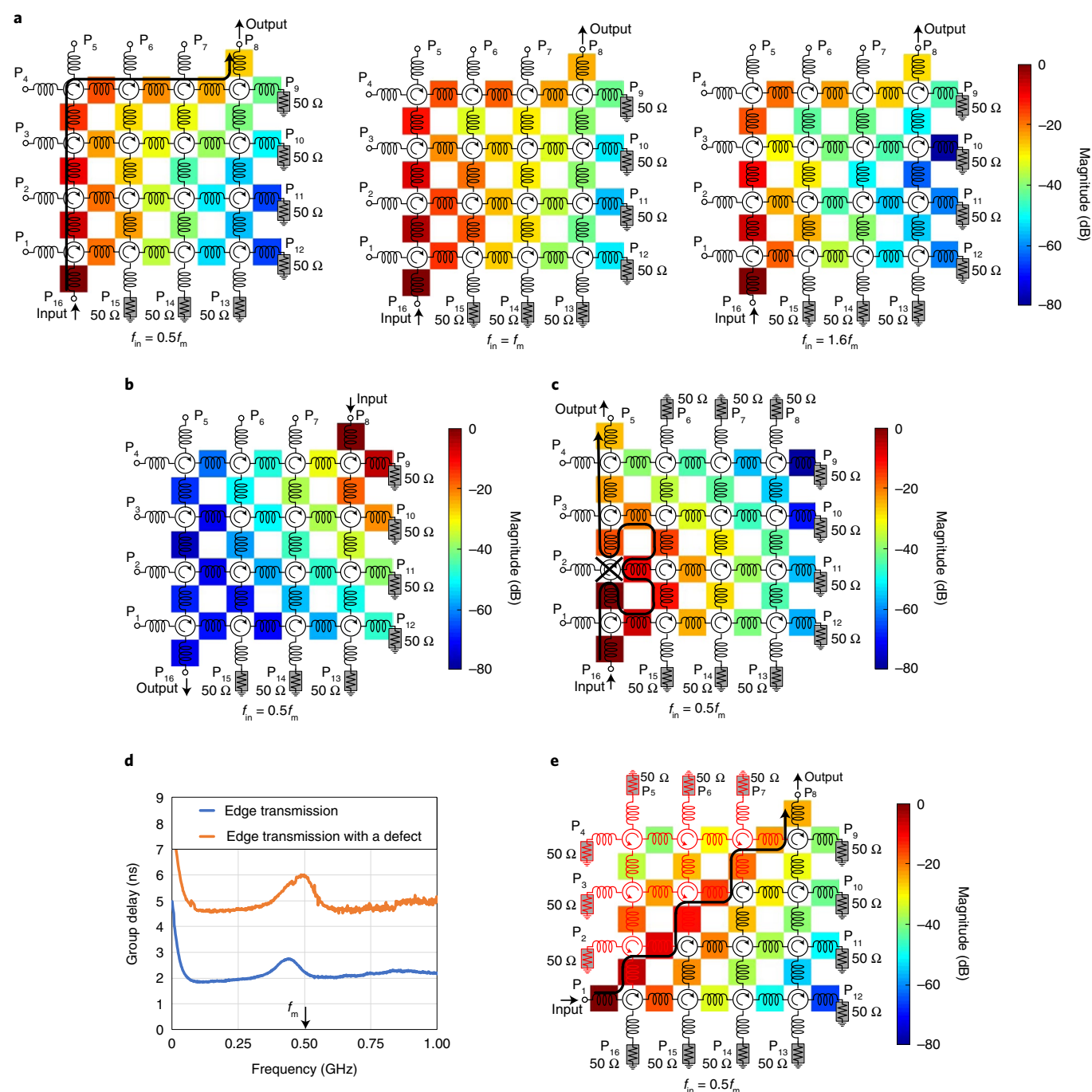


Fig. 4 | Measured field distributions in the decibel scale of the signal travelling through the lattice. a, In line with the lattice topology (CW direction, P₁₆ to P₈) across a wide frequency range. **b**, In the opposite direction of the lattice topology (CCW direction, P₈ to P₁₆). **c**, Along the edge mode in the presence of an artificially induced defect by turning off a unit cell along the edge. **d**, Transmission group delays with and without the artificially induced defect, showing the longer path taken by the signal around the defect. **e**, Measured field distributions of the signal travelling along the domain wall created by choosing different handedness for the unit cells on either side of the domain wall.

larger fractional bandwidth than any other time-invariant and/or time-variant photonic TI (Fig. 3c). For instance, the TI discussed in ref. ¹⁶ achieves topological edge protection across a bandwidth of 0.270 GHz and operating at around 4.485 GHz, leading to a fractional bandwidth of ~6%. Finally, in ref. ²⁵, the proposed acoustic Floquet TI achieves topological protection over ~0.5 kHz and operating around a centre frequency of ~22 kHz, thereby leading to a fractional bandwidth of ~2.2%. On the other hand, our experiment demonstrates wideband topological protection, ranging from d.c.

to 1 GHz, with a fractional bandwidth of 200%. Interestingly, the upper frequency limit in our implementation is only determined by the specific switching technology at hand, and it may be further extended using different CMOS platforms.

We validated the robustness of our non-reciprocal Floquet TI to lattice disorders and defects in experiments, by artificially inducing a drastic defect, that is, turning off one of the lattice nodes along the edge (Fig. 4c). In contrast to the topologically trivial lattice, the signal propagation in our Floquet TI is unaffected even in the absence

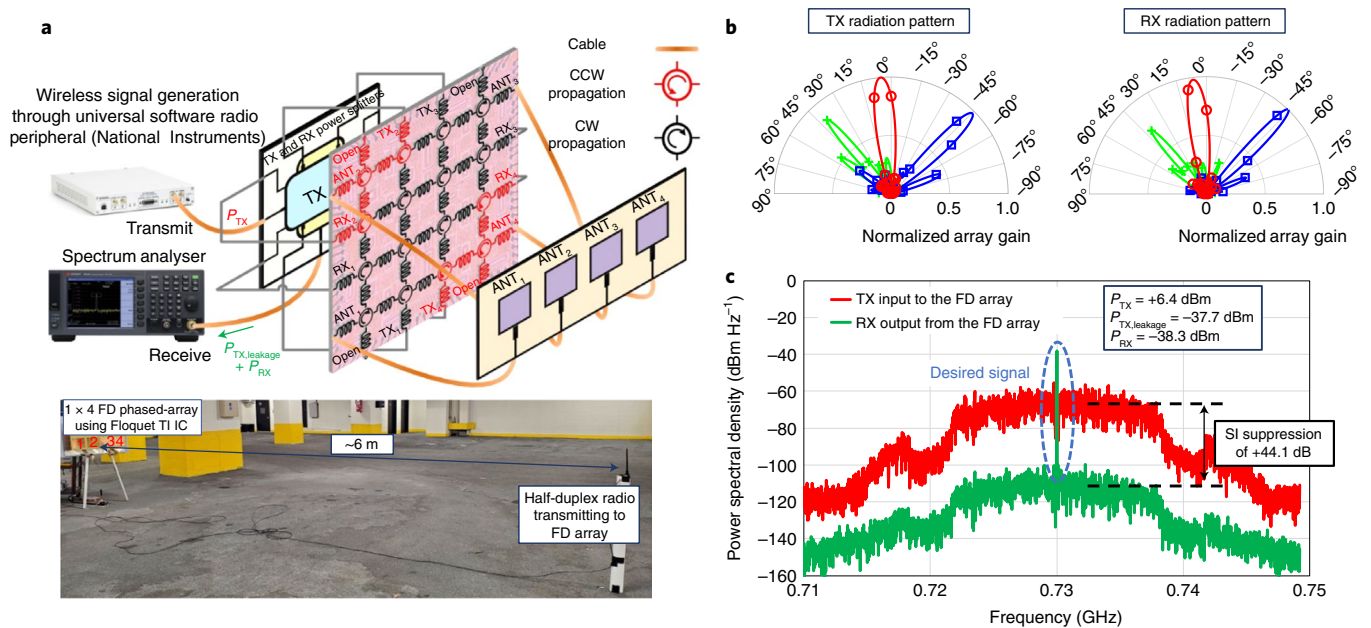


Fig. 5 | Wireless demonstration of a four-element 730 MHz FD phased array where four transmitters (TX), receivers (RX) and antennas (ANT) are interfaced through our reconfigurable CMOS Floquet TI IC. **a**, Experimental setup and wireless link performing over-the-air FD communication. **b**, Transmitter and receiver beam-steering performance obtained by leveraging the programmable delays provided by the Floquet TI lattice. Each colour depicts an array radiation pattern steered towards a different angle of transmission/reception, namely, -45° (blue), 0° (red) and 45° (green). **c**, Measured desired signal and transmitter self-interference when the transmitter and receiver arrays are steered to $+45^\circ$ and 0° , respectively. When transmitting a 20 MHz, OFDM-QPSK signal with a total transmit power of $+6.4$ dBm, we measured an array self-interference suppression of $+44.1$ dB, enabling the simultaneous reception of a $+10$ dBm continuous-wave signal transmitted from a dipole antenna 6 m away with ~ 0 dB SINR. P_{TX} , transmitter power; P_{RX} , received power; $P_{TX,leakage}$, transmitter leakage at the receiver output; SI, self-interference.

of one of the unit cells due to the topological nature of the lattice. As noticed through the field distributions, the signal travels around the defect (Fig. 4c, signal path), thus preserving the anomalous topological phase and isolation across the bulk. Transmission around the defect results in a longer transmission path, as evidenced by the increase in group delay (Fig. 4d).

Our reconfigurable Floquet TI can also create reflection-less tailored domain walls of arbitrary shape, thus providing great control over wave propagation and multiplexing opportunities. For instance, Fig. 4e shows a tailored domain-wall boundary created between two points, with arbitrary shape, by reversing the propagation direction of the elements on one side of the boundary. The signal propagates robustly along the domain wall without penetrating into the bulk on either side.

5G wireless FD phased-array applications

Wide bandwidth, reconfigurable signal routing, non-reciprocal isolation, wideband nanosecond-scale delays and robustness to defects offered by our Floquet TI platform, along with its implementation in a CMOS chip, open a plethora of real-world applications in wireless communications, radar and quantum information processing. FD phased-array³⁹ and multi-input multi-output⁴⁰ systems are exciting technologies that combine the two times capacity benefit from FD capability^{41–43} with the beamforming and spatial multiplexing gains of multi-antenna systems. However, the main challenge in these systems is the handling of complex self-interference between every transmitter–receiver pair, causing the complexity of the self-interference cancellation circuitry to scale as $O(M^2)$, where M is the number of antennas⁴⁰.

An FD phased-array experiment involving our CMOS TI is shown in Fig. 5a, where four transmitters, receivers and patch antennas operating at 730 MHz are interfaced with the Floquet TI modulated at 500 MHz. By programming the clock delays within

each lattice element, programmable delays of $2f_m/8$ – $9f_m/8$, or 360° phase shifting at frequencies greater than f_m , are introduced between each transmitter/receiver and its antenna, allowing for complete, simultaneous and independent transmitter/receiver beamforming. At the same time, the TI ensures isolation between every transmitter–receiver pair, enabling enhanced self-interference suppression. Measured phased-array beam patterns for the transmitter and receiver arrays are shown in Fig. 5b for normal, $+45^\circ$ and -45° steering. With the transmitter and receiver arrays configured for $+45^\circ$ and 0° steering, respectively, the overall array isolation measured from the transmitter power-splitter input to the receiver power-combiner output (calibrating out the losses of the splitter and combiner) is $+44.1$ dB (Fig. 5c), enabling the simultaneous reception of a $+10$ dBm continuous-wave signal transmitted from a dipole antenna 6 m away with ~ 0 dB signal-to-interference-plus-noise-ratio (SINR). Compared with state-of-the-art multi-antenna FD systems^{39,40}, which achieve ~ 15 dB transmitter-to-receiver isolation at the antenna interface, our prototype achieves up to 30 dB higher isolation, thereby greatly relaxing the dynamic-range requirements of the subsequent receiver. Introducing additional 50 dB of self-interference cancellation using conventional radio-frequency/analogue and digital techniques can enable 600-m-link range at 10 dB SINR assuming traditional Friis transmission path loss, thus showcasing the powerful impact of our CMOS TI as a programmable multi-antenna interface for FD phased-array wireless systems.

Ultrawideband TTD beamforming for impulse radar

Ultrawideband impulse radars find application in indoor object detection, positioning and tracking^{44,45}, and they require tunable, wideband TTDs. Realizing these nanosecond-scale delays in integrated circuit (IC) implementations has been challenging, due their large form factor and high insertion loss⁴⁵. Again, our dispersion-free CMOS Floquet TI offers unique features in terms

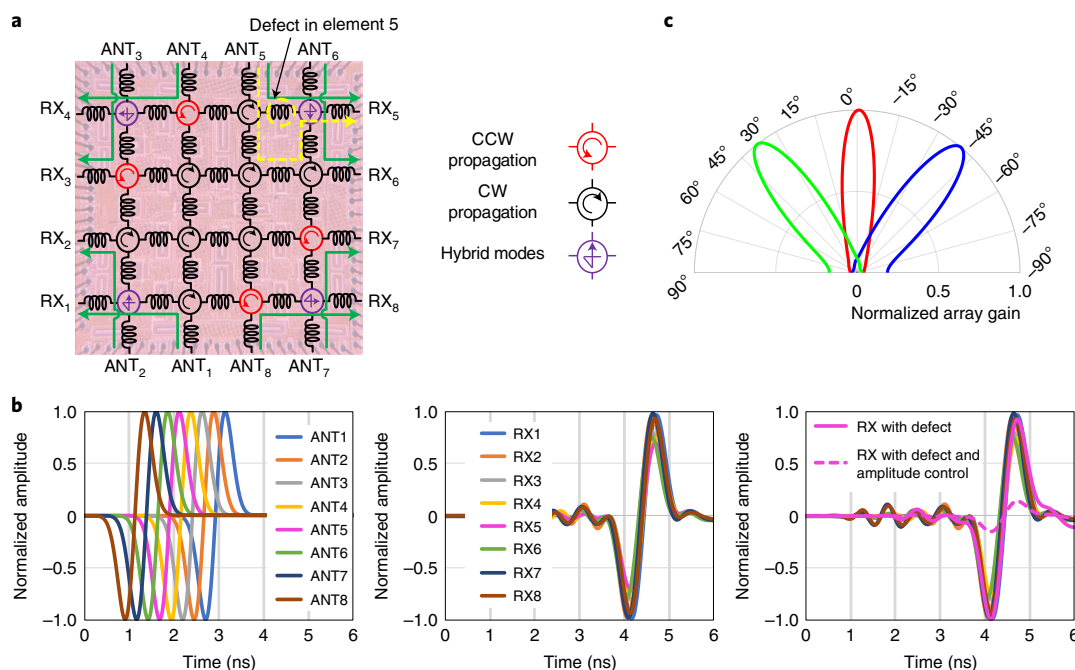


Fig. 6 | Floquet TI leveraged as a reconfigurable antenna interface for an eight-element wideband, TTD beamformer. **a**, Configuration diagram of the Floquet TI lattice when programmed for wideband, TTD beamforming between eight receiver ports and eight antenna ports connected to a 1×8 antenna array. The green and yellow paths depict the signal paths with and without a defect, which is artificially induced by turning off the switches in the fifth beamforming path. **b**, Time-domain simulation for an eight-element array with antenna spacing of 12 cm using the measured scattering parameters of the Floquet TI. Time-shifted Gaussian monopulse waveforms with a carrier frequency of 730 MHz and a -3 dB bandwidth of 860 MHz are incident at the antenna ports to emulate an excitation at -40° angle of arrival. In the presence of an artificially induced defect, the signal travels around it, preserving the signal propagation and beamforming capabilities. **c**, Synthesized wideband beam patterns provided by the Floquet TI (without the defect) when the programmable delays are configured for normal, $+40^\circ$ and -40° steering.

of reconfigurable signal routing with programmable wideband nanosecond-scale delays, ideally suited to support TTD beamforming across multiple antennas and transmitters/receivers (Fig. 6a) for a system with eight elements. Each antenna–receiver pair consists of two circulator elements in the signal path, where one element is operated in the CW/CCW mode and can offer its entire delay coverage ranging from $T_m/8$ – $7T_m/8$, whereas the other element is operated in a hybrid configuration, namely, $T_1 \rightarrow T_3 \rightarrow T_2 \rightarrow T_4$, and is shared across two antenna–receiver pairs; this results in delays ranging from $T_m/8$ to $3T_m/8$ for each pair. Therefore, a modulation frequency of 500 MHz leads to a programmable delay in each antenna–receiver pair ranging from 500 ps to 2.5 ns with a -3 dB bandwidth of 1.25 GHz.

Our Floquet TI operates well beyond the DBW product trade-off of conventional linear time-invariant electromagnetic structures³⁴. This is remarkably different from conventional photonic TIs, which experience a drastic trade-off between the bandgap opening and achievable delay sustained by the edge states. In our platform, the maximum delay imparted by a single unit cell is approximately equal to the clocking time period ($(\frac{N-1}{N})T_s \approx T_s$ for large N) and the signal bandwidth is proportional to the number of parallel layers (N) times the clocking frequency (f_s) (-3 dB bandwidth, $\sim 0.375Nf_s$). This leads to a DBW product that is proportional to the number of parallel layers (N) in the unit cell (DBW, $\sim 0.375(N-1)$). For reference, the unit cells of our lattice are implemented using eight parallel paths, imparting a maximum delay of 1.75 ns with a -3 dB bandwidth of 1.4 GHz. Therefore, our experimentally demonstrated DBW product is 2.45, which is close to the theoretical DBW product of an eight-path unit element (theoretical DBW = $0.375 \times 7 = 2.62$). Implementing a device with a larger number of parallel layers increases the DBW value of our Floquet TI.

TTD systems are typically characterized using two metrics: the DBW–miniaturization factor product and the noise figure. Our Floquet TI lattice exhibits a DBW–miniaturization factor product that is several orders of magnitude larger than passive implementations^{46,47} and lower noise figure compared with active implementations⁴⁸. For instance, earlier passive TTD proposals that relied on quasi-distributed LC networks can impart a maximum delay of 400 ps (ref. ⁴⁶) or 180 ps (ref. ⁴⁷) across a -3 dB bandwidth of 13.0 GHz (ref. ⁴⁶) or 7.6 GHz (ref. ⁴⁷) and occupying a chip area of 2.5 mm^2 (ref. ⁴⁶) or 1.0 mm^2 (ref. ⁴⁷), namely, a miniaturization factor ($\lambda_{\text{centre}}^2/\text{area}$) of 4×10^2 (ref. ⁴⁶) or 2×10^3 (ref. ⁴⁷), thereby resulting in a DBW–miniaturization factor product of 2.0×10^3 (ref. ⁴⁶) or 2.7×10^3 (ref. ⁴⁷), respectively. In comparison, our prototype can impart a maximum delay of 2.5 ns over a -3 dB bandwidth of 1.25 GHz and occupying a chip area of 1.5 mm^2 per channel (that is, a miniaturization factor of 2.4×10^5), resulting in a DBW–miniaturization factor product of 7.5×10^5 , which is 10^2 – 10^3 times higher compared with earlier passive proposals. On the other hand, the earlier active-delay implementation in ref. ⁴⁸ can also achieve a comparable DBW–miniaturization factor product, but it exhibits a large noise figure of 17.5–23.0 dB. In comparison, our prototype achieves a noise figure of 6–9 dB, which is up to 12 dB or 15.8 times lower, thereby advancing the state of the art in TTD system performance.

Figure 6b shows a time-domain simulation obtained using the measured scattering parameters of our Floquet TI for a 1×8 antenna array with a free-space path distance of 12 cm between two consecutive antennas. Here an ultrawideband monopulse radar signal⁴⁴ with a carrier frequency of 730 MHz and a -3 dB bandwidth of 830 MHz is time shifted and incident on the antenna ports to emulate a -40° angle of arrival. The Floquet TI compensates for the delay difference between the antennas and enables constructive summation across

all the receiver ports (Fig. 6b). In the presence of a defect, which is artificially induced by turning off the switches in the fifth beam-forming path ($\text{ANT}_5\text{--RX}_5$), the signal travels around the defect due to topological robustness, thereby preserving signal propagation and beamforming capabilities. Figure 6a,b also depicts the transmission path and output signals at the receiver ports in the presence of a defect in the fifth beamforming path. Adjusting the delays in the unit cells enables achieving the desired delay despite the longer transmission path, and the insertion loss due to this longer path can be compensated using amplitude/gain control⁴⁵. Through our programmable delays, the beam pattern of such a 1×8 ultrawideband array can be steered from $+40^\circ$ to -40° , and the synthesized array gain patterns, without the defect, based on the measured scattering parameters for normal, $+40^\circ$ and -40° steering directions (Fig. 6c).

Conclusions

We have reported a non-reciprocal photonic Floquet TI based on an array of quasi-electrostatic synthetically rotating circuit elements, and demonstrated its use in practical 5G wireless systems. Our implementation offers orders of magnitude broader bandwidth than previous photonic TI systems. It also fits within a compact, subwavelength form factor, overcoming challenges associated with the distribution of the modulation signal and allowing integration into a CMOS chip. The results provide a route to practical applications of reconfigurable TIs as reciprocal/non-reciprocal signal multiplexers for wireless communication systems, radar and quantum information processing systems. Initially, two experiments were conducted to illustrate the practical relevance of our Floquet TI: it was used as a robust and reconfigurable antenna interface for 5G FD phased-array wireless, and it was used for ultrawideband impulse radar beamforming. Similar operations can be envisioned to interface a multitude of qubits to excitation and readout circuitry in quantum computing applications.

Methods

CMOS implementation. Floquet TI is implemented as a lattice of 4×4 helicoidally rotating quasi-electrostatic circulator unit cells. Each layer of the four-port, eight-layered unit circulator consists of a 2.5 pF shunt capacitor connected to four ports through $50\text{ }\mu\text{m}/40\text{ nm}$ transistor switches. The on resistance of these transistor switches is $\sim 5.6\text{ }\Omega$. The coupling inductors between the unit circulators are implemented on chip using four-turn lumped inductors with stacked metal layers to achieve a compact area and low resistive losses. The bulk nodes of our Floquet TI are connected to unity-gain buffers whose outputs are multiplexed to a pad for the measurement of field distributions (Figs. 4 and 5). The clocking circuitry consists of pseudo-differential buffers to generate square waves from the input 2 GHz differential sinusoidal signals. These 2 GHz square-wave signals were divided by a factor of 4 and then fed to a non-overlapping clock generator to generate the eight phases of 500 MHz and 12.5% duty cycle non-overlapping clocks that drive the switches in the circulators.

Discussion of loss effects. A critical parameter that governs practical applicability is the insertion loss. A single circulator element within the lattice exhibits a transmission loss of 4.0–5.5 dB to the next port, isolation of 15–20 dB to the following port and 25–35 dB to the subsequent ports (Fig. 3a). Out of the loss of 4.0–4.5 dB, harmonic conversion loss contributes $\sim 1.0\text{--}1.5\text{ dB}$ and the remaining $\sim 3.0\text{--}3.5\text{ dB}$ arises from parasitic contributors. As the signal propagates through multiple elements, the parasitic contributions accumulate, whereas the contribution of harmonic conversion losses does not increase (Supplementary Sections 1B and 4). It should be noted that the parasitic loss of $3.0\text{--}3.5\text{ dB}$ per unit cell can be reduced through the use of scaled CMOS technology nodes that offer transistors with reduced on resistance and parasitic capacitance. In the limit, as the contribution of these parasitic losses becomes negligible, the loss from harmonic conversion is the only contributor, and it improves with the number of parallel layers N . Hence, ideally, a lattice of arbitrarily large size can be realized with a low insertion loss of $\sim 1.0\text{--}1.5\text{ dB}$ (corresponding to the harmonic conversion loss of a single element) as CMOS technology scales.

5G wireless FD phased-array experiment. The measurement setup for the FD phased-array experiment involving our CMOS TI is shown in Fig. 6a, where four transmitters, receivers and patch antennas operating at 730 MHz are interfaced with the Floquet TI modulated at 500 MHz. The four transmitter ports are fed from a universal software radio peripheral generating $+11\text{ dBm}$, 20 MHz, orthogonal

frequency division multiplexing (OFDM)–quadrature phase shift keying (QPSK) signal that is power split four ways, resulting in $+0.4\text{ dBm}$ incident on each transmitter port (total power of $+6.4\text{ dBm}$ across four elements), whereas the four receiver ports are combined and monitored on a spectrum analyser.

Data availability

The data that support the findings of this study are available from the corresponding authors upon reasonable request.

Received: 17 December 2021; Accepted: 18 March 2022;

Published online: 2 May 2022

References

- Hasan, M. Z. & Kane, C. L. Colloquium: topological insulators. *Rev. Mod. Phys.* **82**, 3045–3067 (2010).
- Moore, J. E. The birth of topological insulators. *Nature* **464**, 194–198 (2010).
- Thouless, D. J., Kohmoto, M., Nightingale, M. P. & Denny, M. Quantized Hall conductance in a two-dimensional periodic potential. *Phys. Rev. Lett.* **49**, 405–408 (1982).
- Kitagawa, T., Berg, E., Rudner, M. & Demler, E. Topological characterization of periodically driven quantum systems. *Phys. Rev. B* **82**, 235114 (2010).
- Lindner, N. H., Refael, G. & Galitski, V. Floquet topological insulator in semiconductor quantum wells. *Nat. Phys.* **7**, 490–495 (2011).
- Cayssol, J., Dóra, B., Simon, F. & Moessner, R. Floquet topological insulators. *Phys. Status Solidi RRL* **7**, 101–108 (2013).
- Rudner, M. S., Lindner, N. H., Berg, E. & Levin, M. Anomalous edge states and the bulk-edge correspondence for periodically driven two-dimensional systems. *Phys. Rev. X* **3**, 031005 (2013).
- Haldane, F. D. M. & Raghu, S. Possible realization of directional optical waveguides in photonic crystals with broken time-reversal symmetry. *Phys. Rev. Lett.* **100**, 013904 (2008).
- Lu, L., Joannopoulos, J. D. & Soljačić, M. Topological photonics. *Nat. Photon.* **8**, 821–829 (2014).
- Khanikaev, A. B. & Shvets, G. Two-dimensional topological photonics. *Nat. Photon.* **11**, 763–773 (2017).
- Ozawa, T. et al. Topological photonics. *Rev. Mod. Phys.* **91**, 015006 (2019).
- Albert, V. V., Glazman, L. & Jiang, L. Topological properties of linear circuit lattices. *Phys. Rev. Lett.* **114**, 173902 (2015).
- Ningyuan, J., Owens, C., Sommer, A., Schuster, D. & Simon, J. Time- and site-resolved dynamics in a topological circuit. *Phys. Rev. X* **5**, 021031 (2015).
- Hofmann, T., Helbig, T., Lee, C. H., Greiter, M. & Thomale, R. Chiral voltage propagation and calibration in a topoelectrical Chern circuit. *Phys. Rev. Lett.* **122**, 247702 (2019).
- Ni, X., Xiao, Z. C., Khanikaev, A. B. & Alu, A. Robust multiplexing with topoelectrical higher-order Chern insulators. *Phys. Rev. Appl.* **13**, 064031 (2020).
- Wang, Z., Chong, Y. D., Joannopoulos, J. D. & Soljačić, M. Observation of unidirectional backscattering-immune topological electromagnetic states. *Nature* **461**, 772–775 (2009).
- Poo, Y., Wu, R. X., Lin, Z. F., Yang, Y. & Chan, C. T. Experimental realization of self-guiding unidirectional electromagnetic edge states. *Phys. Rev. Lett.* **106**, 093903 (2011).
- Chen, W. J. et al. Experimental realization of photonic topological insulator in a uniaxial metacrystal waveguide. *Nat. Commun.* **5**, 5782 (2014).
- Cheng, X. J. et al. Robust reconfigurable electromagnetic pathways within a photonic topological insulator. *Nat. Mater.* **15**, 542–548 (2016).
- Hafezi, M., Demler, E. A., Lukin, M. D. & Taylor, J. M. Robust optical delay lines with topological protection. *Nat. Phys.* **7**, 907–912 (2011).
- Fang, K. J., Yu, Z. F. & Fan, S. H. Realizing effective magnetic field for photons by controlling the phase of dynamic modulation. *Nat. Photon.* **6**, 782–787 (2012).
- Rechtsman, M. C. et al. Photonic Floquet topological insulators. *Nature* **496**, 196–200 (2013).
- Gorlach, M. A. et al. Far-field probing of leaky topological states in all-dielectric metasurfaces. *Nat. Commun.* **9**, 909 (2018).
- Khanikaev, A. B., Fleury, R., Mousavi, S. H. & Alu, A. Topologically robust sound propagation in an angular-momentum-biased graphene-like resonator lattice. *Nat. Commun.* **6**, 8260 (2015).
- Fleury, R., Khanikaev, A. B. & Alu, A. Floquet topological insulators for sound. *Nat. Commun.* **7**, 11744 (2016).
- Mukherjee, S. et al. Experimental observation of anomalous topological edge modes in a slowly driven photonic lattice. *Nat. Commun.* **8**, 13918 (2017).
- Maczewsky, L. et al. Observation of photonic anomalous Floquet topological insulators. *Nat. Commun.* **8**, 13756 (2017).
- Tymchenko, M. & Alu, A. Circuit-based magnetless Floquet topological insulator. In *2016 10th International Congress on Advanced Electromagnetic Materials in Microwaves and Optics (METAMATERIALS)* 373–375 (IEEE, 2016).

29. Darabi, A., Ni, X., Leamy, M. & Alu, A. Reconfigurable Floquet elastodynamic topological insulator based on synthetic angular momentum bias. *Sci. Adv.* **6**, eaba8656 (2020).
30. Peng, Y. G. et al. Experimental demonstration of anomalous Floquet topological insulator for sound. *Nat. Commun.* **7**, 13368 (2016).
31. Hu, W. et al. Measurement of a topological edge invariant in a microwave network. *Phys. Rev. X* **5**, 011012 (2015).
32. Gao, F. et al. Probing topological protection using a designer surface plasmon structure. *Nat. Commun.* **7**, 11619 (2016).
33. Nagulu, A., Tymchenko, M., Alù, A. & Krishnaswamy, H. Ultra compact, ultra wideband, d.c.-1GHz CMOS circulator based on quasi-electrostatic wave propagation in commutated switched capacitor networks. In *2020 IEEE Radio Frequency Integrated Circuits Symposium (RFIC)* 55–58 (IEEE, 2020).
34. Tymchenko, M., Sounas, D., Nagulu, A., Krishnaswamy, H. & Alù, A. Quasielectrostatic wave propagation beyond the delay-bandwidth limit in switched networks. *Phys. Rev. X* **9**, 031015 (2019).
35. Estep, N. A., Sounas, D. L., Soric, J. & Alu, A. Magnetic-free non-reciprocity and isolation based on parametrically modulated coupled-resonator loops. *Nat. Phys.* **10**, 923–927 (2014).
36. Reiskarimian, N. & Krishnaswamy, H. Magnetic-free non-reciprocity based on staggered commutation. *Nat. Commun.* **7**, 11217 (2016).
37. Chalker, J. T. & Coddington, P. D. Percolation, quantum tunnelling and the integer Hall effect. *J. Phys. C Solid State Phys.* **21**, 2665–2679 (1988).
38. Liang, G. Q. & Chong, Y. D. Optical resonator analog of a two-dimensional topological insulator. *Phys. Rev. Lett.* **110**, 203904 (2013).
39. Dastjerdi, M. B., Reiskarimian, N., Chen, T., Zussman, G. & Krishnaswamy, H. Full duplex circulator-receiver phased array employing self-interference cancellation via beamforming. In *2018 IEEE Radio Frequency Integrated Circuits Symposium (RFIC)* 108–111 (IEEE, 2018).
40. Dastjerdi, M. B., Jain, S., Reiskarimian, N., Natarajan, A. & Krishnaswamy, H. Analysis and design of a full-duplex two-element MIMO circulator-receiver with high TX power handling exploiting MIMO RF and shared-delay baseband self-interference cancellation. *IEEE J. Solid-State Circuits* **54**, 3525–3540 (2019).
41. Zhou, J. et al. Integrated full duplex radios. *IEEE Commun. Mag.* **55**, 142–151 (2017).
42. Katanbaf, M., Chu, K., Zhang, T., Su, C. & Rudell, J. C. Two-way traffic ahead: RF/analog self-interference cancellation techniques and the challenges for future integrated full-duplex transceivers. *IEEE Microw. Mag.* **20**, 22–35 (2019).
43. Dinc, T. et al. Synchronized conductivity modulation to realize broadband lossless magnetic-free non-reciprocity. *Nat. Commun.* **8**, 795 (2017).
44. Immoreev, I. & Fedotov, D. V. Ultra wideband radar systems: advantages and disadvantages. In *2002 IEEE Conference on Ultra Wideband Systems and Technologies (IEEE Cat. No. 02EX580)* 201–205 (IEEE, 2002).
45. Roderick, J., Krishnaswamy, H., Newton, K. & Hashemi, H. Silicon-based ultra-wideband beam-forming. *IEEE J. Solid-State Circuits* **41**, 1726–1739 (2006).
46. Chu, T., Roderick, J. & Hashemi, H. An integrated ultra-wideband timed array receiver in 0.13 μm CMOS using a path-sharing true time delay architecture. *IEEE J. Solid-State Circuits* **42**, 2834–2850 (2007).
47. Rajesh, N. & Pavan, S. Design of lumped-component programmable delay elements for ultra-wideband beamforming. *IEEE J. Solid-State Circuits* **49**, 1800–1814 (2014).
48. Mondal, I. & Krishnapura, N. A 2-GHz bandwidth, 0.25–1.7 ns true-time-delay element using a variable-order all-pass filter architecture in 0.13 μm CMOS. *IEEE J. Solid-State Circuits* **52**, 2180–2193 (2017).

Acknowledgements

This work was supported by the DARPA SPAR program (H.K. and A.A.), the AFOSR MURI program (H.K. and A.A.), the Office of Naval Research (A.A.) and the Department of Defense (A.A.). X.N. thanks Y. Peng for the helpful discussion.

Author contributions

A.N., A.K., A.A. and H.K. initiated the research. A.N. and A.K. simulated and taped out the device. X.N., A.N., A.K. and M.T. conducted the theoretical analysis. A.N. and S.G. conducted the experiments. H.K. and A.A. supervised the research. All the authors wrote the manuscript. A.N., X.N. and A.K. contributed equally to this manuscript.

Competing interests

The authors declare no competing interests.

Additional information

Supplementary information The online version contains supplementary material available at <https://doi.org/10.1038/s41928-022-00751-9>.

Correspondence and requests for materials should be addressed to Andrea Alù or Harish Krishnaswamy.

Reprints and permissions information is available at www.nature.com/reprints.

Publisher's note Springer Nature remains neutral with regard to jurisdictional claims in published maps and institutional affiliations.

© The Author(s), under exclusive licence to Springer Nature Limited 2022